Supplementary Materials for

Stereocontrol on Helical Bimetallic DNA Catalysts with Switchable Enantioselectivity via Dynamic Reaction Distance Regulation

Authors: Jie Sheng[1,3†], Kelly Kar Yun Koh[1,†], Zihan Li[2,†], Jingyi Liu[2,†], Qi Shi[1], Yang Zheng[1], Xinglong Zhang[2]*, Ru-Yi Zhu[1]*

[1]Department of Chemistry, National University of Singapore, Singapore 117544, Singapore.

[2]Department of Chemistry, The Chinese University of Hong Kong, Shatin, Hong Kong 999077, P. R. China.

[3]School of Pharmacy, Nanjing University of Chinese Medicine, Nanjing 210023, P. R. China.

*Corresponding author: xinglong.zhang@cuhk.edu.hk; rzhu@nus.edu.sg;

[†]These authors contributed equally to this work.

Computational Section

1 Density functional theory (DFT) calculations

Given the two unpaired electrons from the two Cu(II) centers, the complex's ground state can be a closed-shell singlet, an open-shell singlet or a triplet. In the closed-shell singlet, the two electrons are paired and occupy same spatial distribution; in the open-shell singlet, the two unpaired electrons have different spatial distributions and exhibit opposite spins; and in the triplet, the two unpaired electrons have parallel spins, with different spatial distributions.

1.1 Benchmarking studies

To determine the ground state of the DNA–catalyst systems, benchmark calculations were performed on one structure each from the adjacent and intervening species. Geometries of the example systems were optimized at GFN2-xTB[15-17] level of theory with *crude* optimization settings, applying the implicit ALPB solvation model with water to mimic the aqueous experimental environment. Both of the example systems were optimized separately in the closed-shell singlet and open-hell triplet states. The open-shell singlet optimization in xTB could not be done as spin-polarized calculation and implicit solvation model are not compatible in the xTB program.

The xTB-optimized structures were subjected to single-point energy calculations using density functional theory (DFT), which were performed using the *Gaussian 16* rev. B.01 program.[18] Two levels of theory were performed on the single point (SP) DFT energy calculations: (i) the BP86 functional[19, 20] with Grimme's D3 dispersion correction[21] with Becke-Johnson damping[22-25] and the 6-311+G(d) basis set[26] for all atoms (denoted as BP86-D3BJ/6-311+G(d)), and (ii) the global-hybrid meta-NGA (nonseparable gradient approximations) MN15 functional[27] with the def2-SVP basis set (denoted as MN15/def2-SVP) for all atoms. Due to some convergence failures in BP86-D3BJ/6-311+G(d), the MN15 functional was selected for its robust performance for transition metal-containing systems[28-35]. The implicit SMD continuum solvation model[36] was used to account for the solvent effect of water in all DFT calculations.

Consequently, the closed-shell singlet, symmetry-broken open-shell singlet and triplet states of example systems were calculated at MN15/def2-SVP level on each xTB-optimized structure. It was found that for the example adjacent system, the open-shell singlet gave the lowest energy, while the triplet and closed-shell singlet were 28.3

kcal/mol and 44.4 kcal/mol higher in energy, respectively. For the example intervening system, the most stable state was also the open-shell singlet, while the triplet and closed-shell singlet were 0.0 kcal/mol (isoenergetic) and 41.0 kcal/mol higher. The near-degeneracy between open-shell singlet and triplet in the intervening system is likely due to the long Cu–Cu distance, resulting in weak orbital overlap and small exchange interaction and thus a small singlet-triplet energy gap. These results indicate that the open-shell singlet represents the ground state, which is consistent with the previous literatures on Cu(II) biradical systems[37, 38].

1.2 Production-level calculations

Based on the preliminary benchmarking calculations, the single point energies for all DNA–catalyst systems were computed at open-shell singlet with SMD(water)UMN15/def2-SVP level of theory, on xTB-optimized geometries with 2 unpaired electrons. The energies are given in kcal/mol and used for discussion throughout. All molecular structures were visualized using *PyMOL* software[39].

2 Model reaction

The model reaction used for the computational study, with the (truncated) optimized DNA sequences, is shown in **Figure S4**. To accommodate the additional positive charges, three POs closest to the active sites were deprotonated such that the full system has overall neutral charge. For computational convenience, the "hairpin" loops were excluded from the models, i.e., only the first seven or eight nucleotide units (including bases, sugars, and phosphates) were included in models (**Figure S4b**).

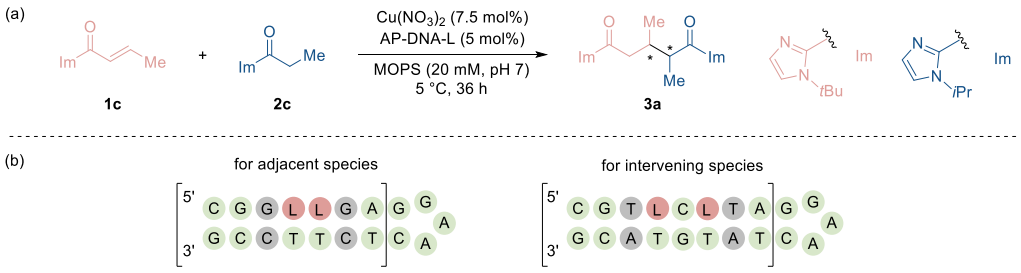

Figure S4. (a) Model reaction used in computational modelling. (b) The DNA sequences of adjacent species (left) and intervening species (right).

3 Naming conventions

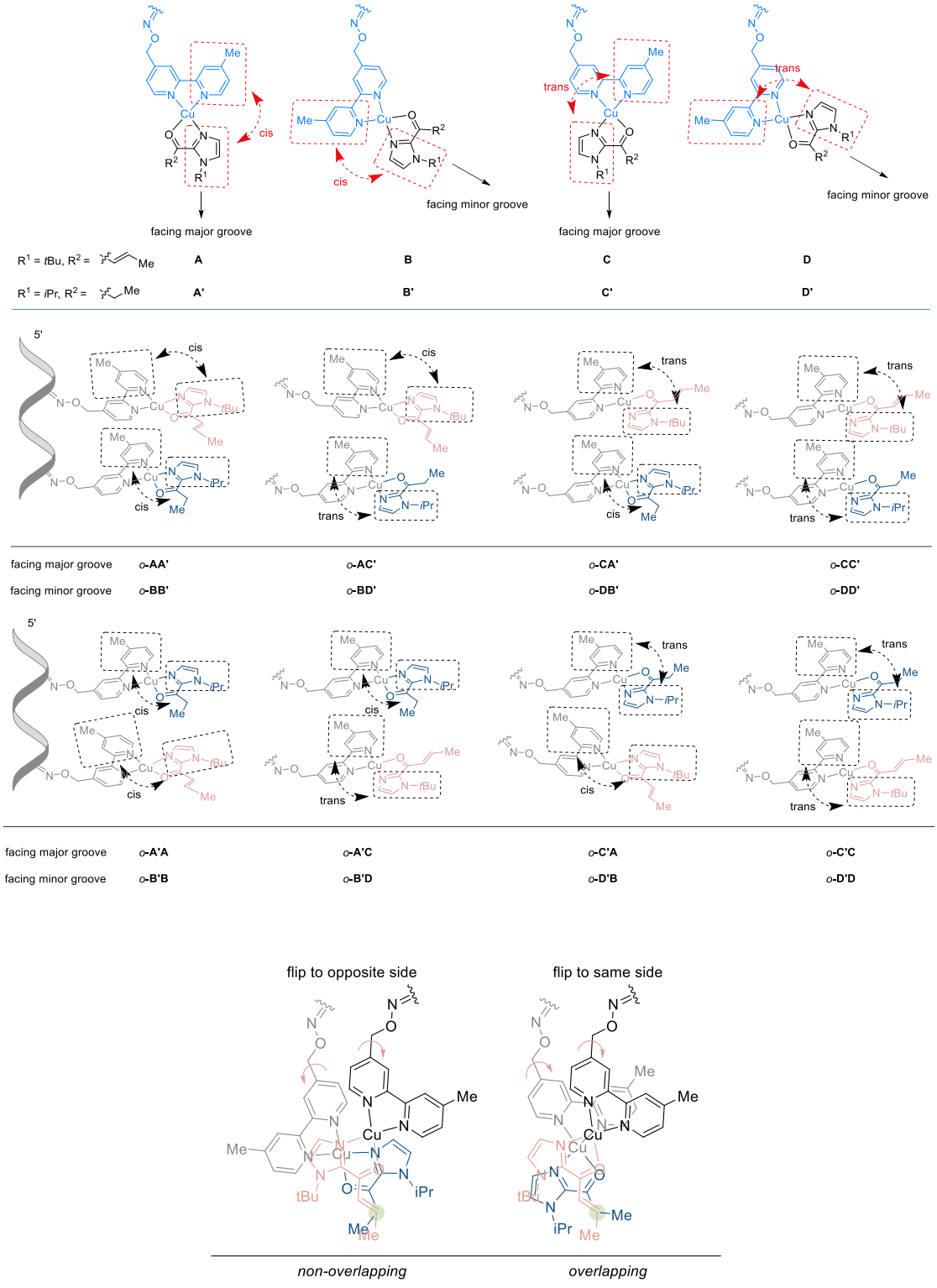

Figure S5. Naming conventions used in computational modelling. For each case, e.g., **AA'**, both *overlapping* and *non-overlapping* cases are possible (shown here only *overlapping*-**AA'**, which we denote as *o*-**AA'**)

We orientate the system with the catalyst-conjugated DNA strand running from the 5'-end to the 3'-end on the left. As shown in **Figure S5**, each system has a name consisting of two capital letters, where the first letter representing the configuration of the fisrt bpy-Cu(II) complex counting from the 5'-end, and the second letter representing the next bpy-Cu(II) complex. The structures are named in such a way (**Figure S5**) that structures where the imidazole group and the 4-methylpyridine are in a *cis* relationship will be **A** or **B**, depending on their orientation towards the DNA groove: if the N (of bpy) atoms face the major groove, it will be **A**; if minor groove, it will be **B**. Similarly, structures where the imidazole group and the 4-methylpyridine are in a *trans* relationship will be **C** or **D**: **C** for major groove and **D** for minor groove. For bpy-Cu(II)-**1c**, unprimed labels (**A** to **D**) are used and for bpy-Cu(II)-**2c**, primed lables are used (**A'** to **D'**).

For all species, combinations of **A** (or **A'**) with **D** (or **D'**), and **B** (or **B'**) with **C** (or **C'**), are not considered, as the likelihood of reaction is minimal when the two bpy-Cu(II) complexes are oriented in opposite directions in those configurations (catalyst-bound substrates point to different grooves). For both of the adjacent species and intervening species, we no longer consider "out states", in which the catalysts remain outside of DNA and the opposite base remains inside the duplex, as their energies are much higher than "in states", where the bpy-conjugated catalyst system tucks inside the dna double helix. When both complexes are oriented toward the major groove, the species are classified as *overlapping* or *non-overlapping* depending on the relative orientation of the two ligands (can be determined based on whether the methyl groups on the ligands are positioned on the same side). The *overlapping* orientation denotes methyl groups on the same side, that they are "overlapping" when viewed along DNA pore top-down, whereas the *non-overlapping* orientation implies that the methyl groups are not overlapped when viewed along the DNA pore. In contrast, when oriented toward the minor groove, only the *overlapping* configuration is possible as *non-overlapping* would face undue steric hindrance.

For example, *overlapping*-**AC'**, which we short-formed as *o*-**AC'** (similarly for all subsequent namings), designates a structure in which (i) both bpy-Cu(II) complexes face the major groove (**A** and **C'**) and have same orientation (*overlapping* methyl groups on ligands); (ii) the ligand arrangement is **A** for bpy-Cu(II)-**1c** and **C'** for bpy-Cu(II) -**2c;** (iii) bpy-Cu(II)-**1c** is nearer the 5′ end than bpy-Cu(II)-**2c** (**A** before **C'**).

All combinations of the orientations were explored during the modelling process.

3.1 Adjacent species

The GFN2-xTB-optimized reactant states of the DNA model system used for the reaction are shown in **Figure S6**, in which the distance between two reaction sites are shown. For structures where a reaction is likely to happen, they were subjected to DFT energy calculations and comparison. The most stable structure is set to be the zero-energy reference. It was found that (1) compared to the distance between two reaction sites, an *overlapping*- or *non-overlapping*- orientation (i.e., whether the methyl groups on the ligands are positioned on the same side) has a more significant impact on energies, likely due to reduced sterics; (2) for overlapping species, structures in which the bpy-Cu(II) complexes share the same configuration (e.g., *o*-**AA'**, *o*-**A'A**, *o*-**BB'**, *o*-**B'B**, *o*-**CC'**, *o*-**CC'**, *o*-**DD'**, and *o*-**D'D**) are typically more favorable for reaction, likely due to effective π-π stacking interactions and favorable geometries. In contrast, other configurations either exhibit higher energies or fail to present a suitable arrangement of the reaction sites/reacting carbon positions. (3) structure *o*-**B'B** exhibits the highest energy (41.5 kcal/mol) among all structures, which can be a result from a combination of steric hindrance within the minor groove and a mismatch between the size of the bpy-Cu(II) complexes and the helical angle of the DNA backbone; (4) structure *o*-**DB'**, although the two bpy-Cu(II) complexes are not fully aligned, still showed a shorter reaction distance than structure *o*-**C'A**. This is likely because steric hindrance within the minor groove (*o*-**DB'**) distorts the geometry sufficiently such that the reacting carbon atoms become closer in distance that those within the major groove (*o*-**C'A**). Thus, despite closer distance between the reacting carbon atoms, the energy may still be high due to strain and distortion of the catalyst within the DNA. This leads to elevated energy (32.3 kcal/mol) as calculated. The most stable structure is *n*-**CC'**, which will yield the (*R*,*R*)-product as observed experimentally.

o-**AA'**	*n*-**AA'**
ΔΔE = 10.9 kcal/mol	*N/C*
d = 5.77 Å	*d* = 7.10 Å
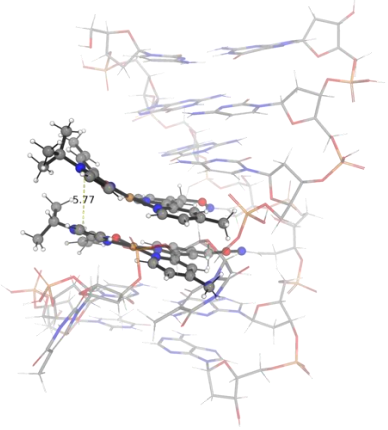	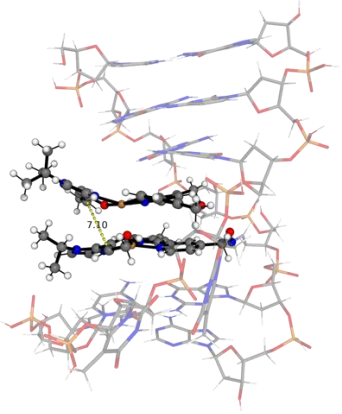
***o*-AC'**	***n*-AC'**
ΔΔE = 20.4 kcal/mol	ΔΔE = 10.2 kcal/mol
d = 4.49 Å	*d* = 6.50 Å
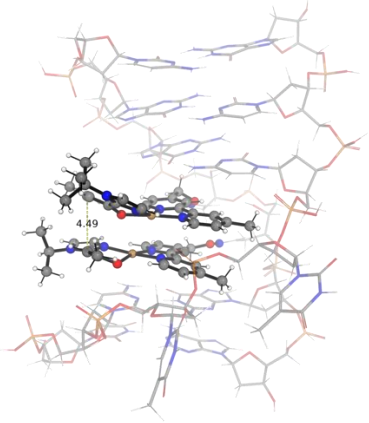	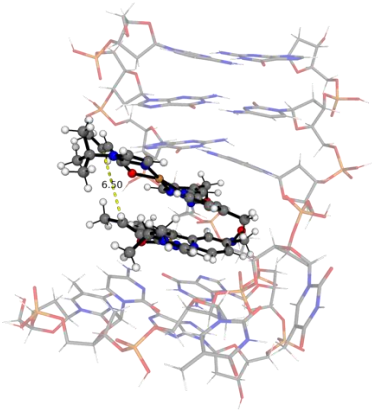
***o*-A'A**	***n*-A'A**
ΔΔE = 1.42 kcal/mol	*N/C*
d = 6.31 Å	*d* = 8.76 Å

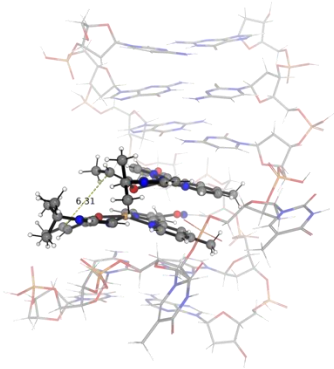	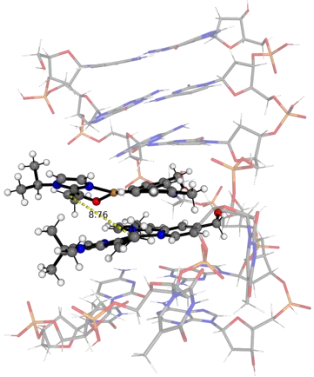
***o*-A'C**	***n*-A'C**
ΔΔE = 9.5 kcal/mol	ΔΔE = 1.2 kcal/mol
d = 4.36 Å	*d* = 4.10 Å
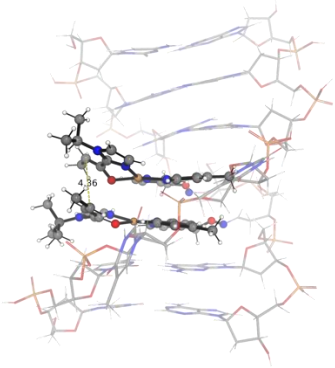	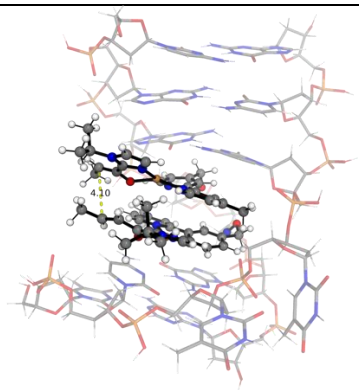
***o*-BB'**	***o*-BD'**
ΔΔE = 28.0 kcal/mol	*N/C*
d = 7.49 Å	*d* = 10.14 Å
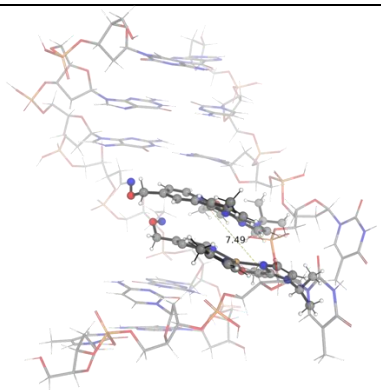	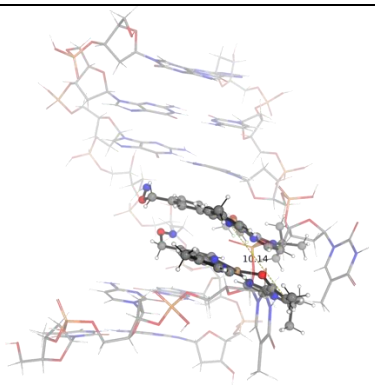
***o*-B'B**	***o*-B'D**
ΔΔE = 41.5 kcal/mol	*N/C*
d = 6.49 Å	*d* = 9.47 Å

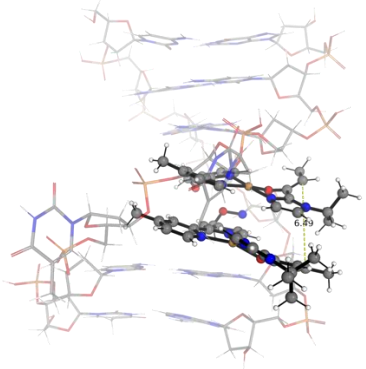	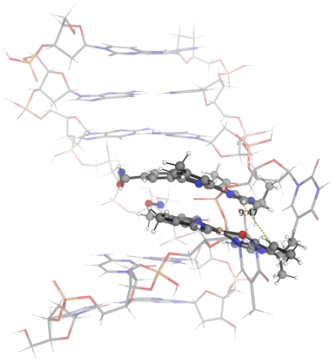
***o*-CA'**	***n*-CA'**
N/C	ΔΔE = 37.6 kcal/mol
d = 7.98 Å	*d* = 5.98 Å
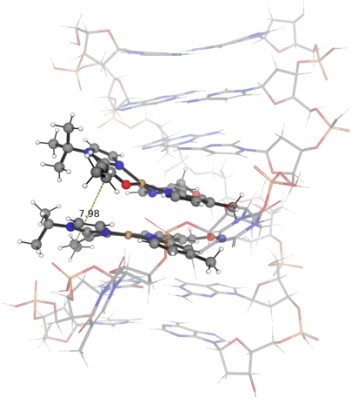	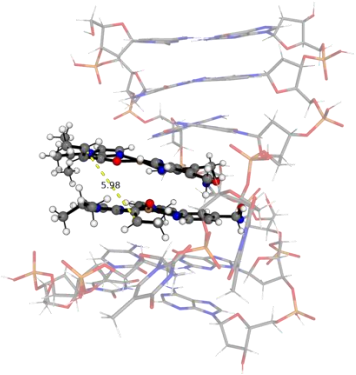
***o*-CC'**	***n*-CC'**
ΔΔE = 19.2 kcal/mol	ΔΔE = 0.0 kcal/mol
d = 3.97 Å	*d* = 4.24 Å
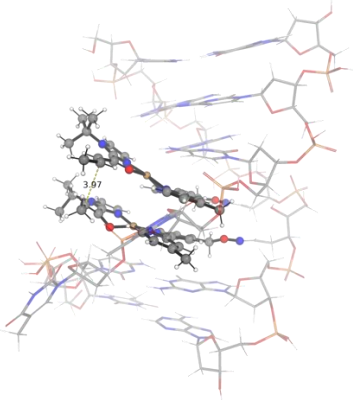	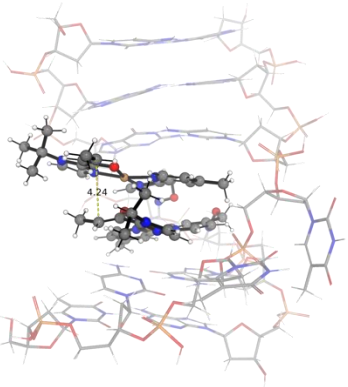
***o*-C'A**	***n*-C'A**
N/C	ΔΔE = 25.1 kcal/mol
d = 8.42 Å	*d* = 5.12 Å

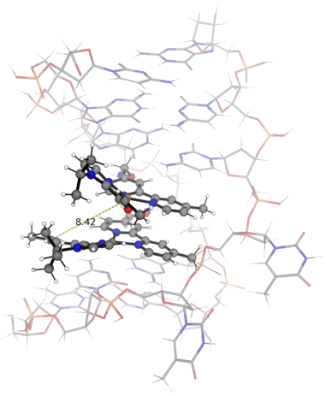	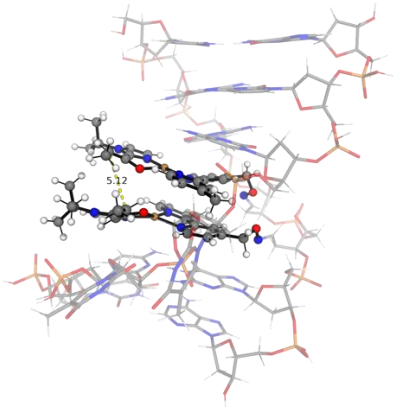
***o*-C'C**	***n*-C'C**
ΔΔE = 16.6 kcal/mol	ΔΔE = 1.7 kcal/mol
d = 3.32 Å	*d* = 3.82 Å
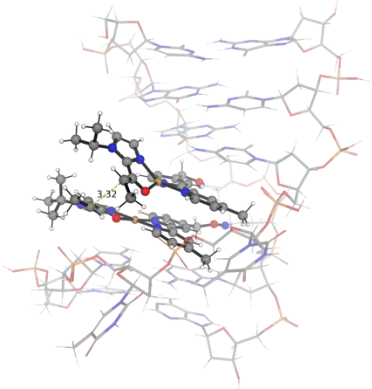	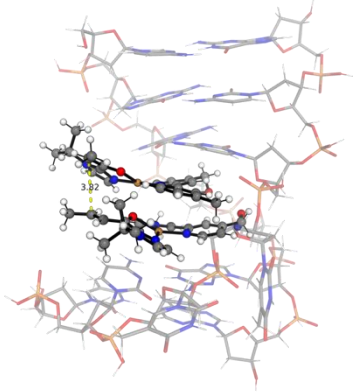
***o*-DB'**	***o*-DD'**
ΔE = 32.3 kcal/mol	ΔE = 15.3 kcal/mol
d = 3.37 Å	*d* = 3.82 Å
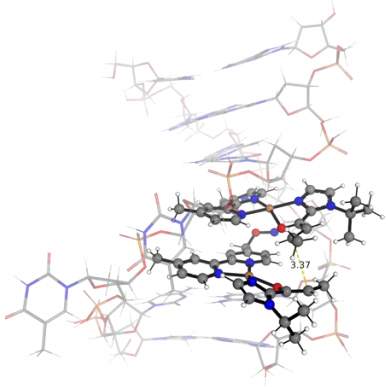	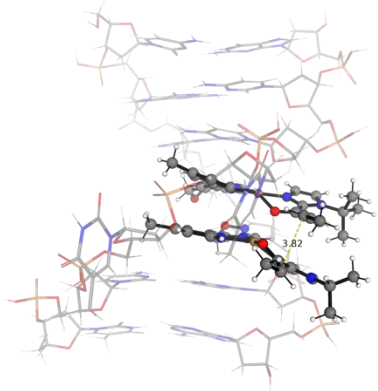
***o*-D'B**	***o*-D'D**
ΔΔE = 26.0 kcal/mol	ΔΔE = 22.7 kcal/mol
d = 4.36 Å	*d* = 5.36 Å

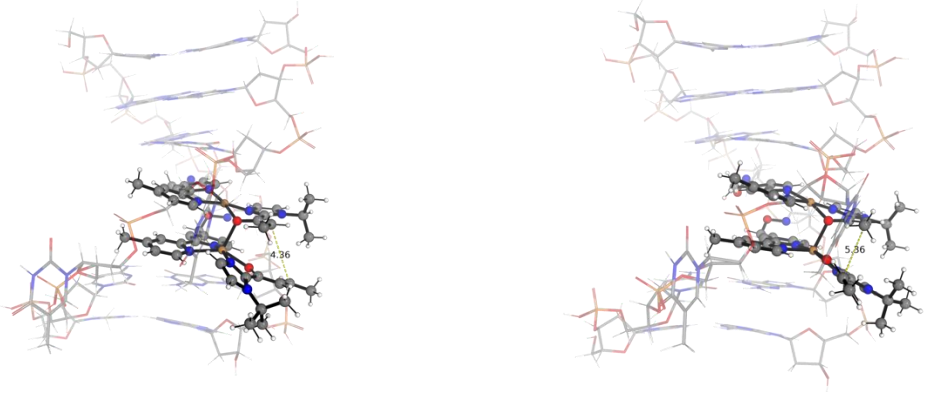

Figure S6. GFN2-xTB-optimized reactant states of the reaction. Relative energy values are given in kcal/mol with respect to the most stable complex. N/C denotes "not calculated" due to the unfeasible geometrical arrangement for product formation.

3.2 Intervening species

The GFN2-xTB-optimized reactant states of the DNA model system used for the reaction are shown in **Figure S7**, in which the distance between two reaction sites are shown. Except for the non-productive structures caused by orientation, all other structures were subjected to DFT energy calculations and comparison. The most stable structure *n*-**AA'** is set to be the zero-energy reference. It was found that (1) due to steric hindrance caused by the DNA helical structure, when the complexes are oriented toward the minor groove, the reactive sites cannot approach each other effectively, only two cases are likely to react (*n*-**DB'** and *n*-**D'B**); (2) in constrast to the adjacent species, the structures in which the two bpy-Cu(II) complexes are oriented in the different direction (i.e., *o*-**AC'**, *o*-**A'C**, *o*-**DB'**, *o*-**D'B**, *n*-**CA'** and *n*-**C'A**) exhibited the shortest distances between reacting carbon atoms; (3) the most stable *n*-**AA'** structure yields a product with *S*-configurations at the reacting carbon centers of **1c** and **2c** substrates, in contrast to the most stable *n*-**CC'** structure from adjacent species (which gives *(R,R)*, section 3.1). This enantioselectivity aligns well with the experimental results.

o-**AA'**	*n*-**AA'**
ΔΔE = 19.7 kcal/mol	ΔΔE = 0.0 kcal/mol
d = 6.57 Å	*d* = 5.30 Å

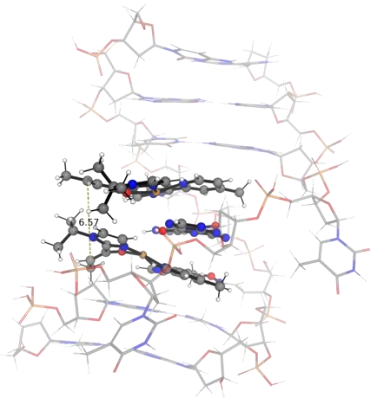	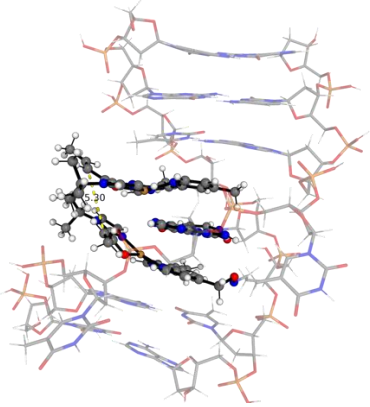
***o*-AC'**	***n*-AC'**
ΔΔE = 100.2 kcal/mol	ΔΔE = 8.6 kcal/mol
d = 4.52 Å	*d* = 6.61 Å
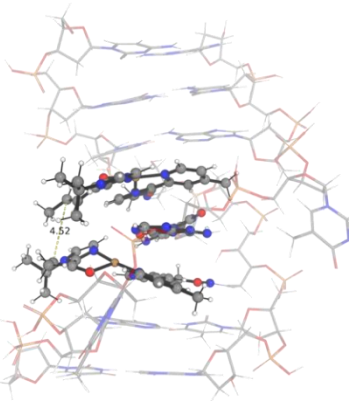	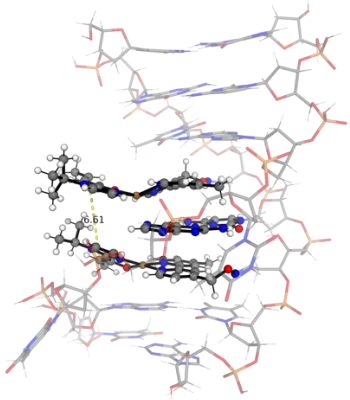
***o*-A'A**	***n*-A'A**
ΔΔE = 22.5 kcal/mol	ΔΔE = 6.8 kcal/mol
d = 7.27 Å	*d* = 5.34 Å
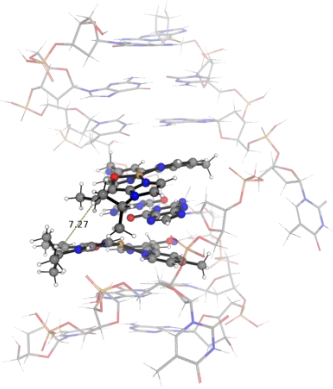	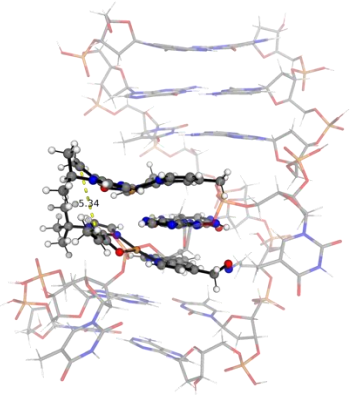
***o*-A'C**	***n*-A'C**
ΔΔE = 24.6 kcal/mol	ΔΔE = 8.3 kcal/mol
d = 3.87 Å	*d* = 6.44 Å

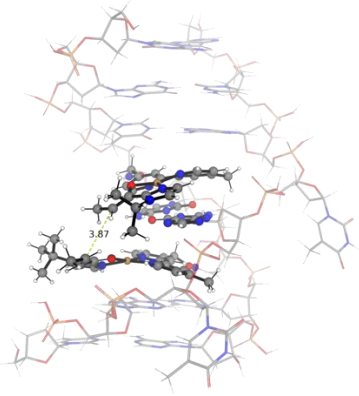	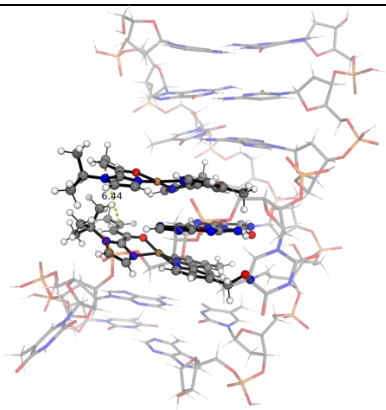
***o*-BB'**	***o*-BD'**
N/C	N/C
d = 12.19 Å	d = 15.33 Å
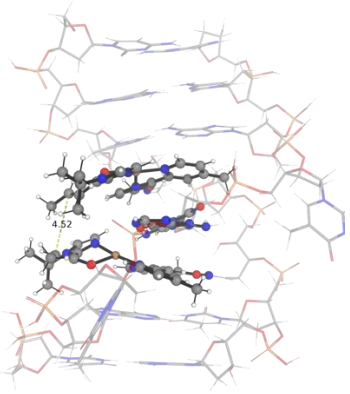	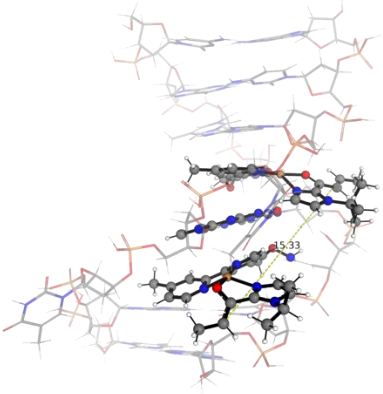
***o*-B'B**	***o*-B'D**
N/C	N/C
d = 11.00 Å	d = 14.64 Å
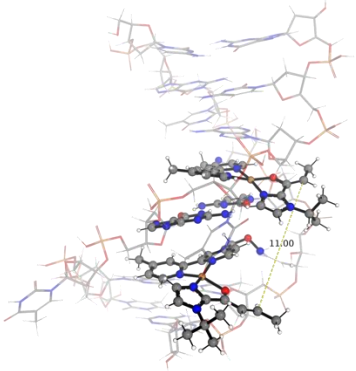	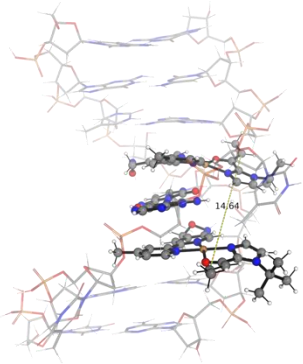
***o*-CA'**	***n*-CA'**
N/C	ΔΔE = 4.9 kcal/mol
d = 10.47 Å	d = 4.87 Å

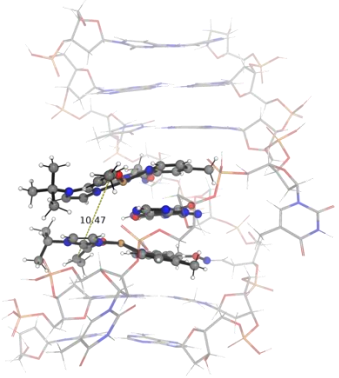	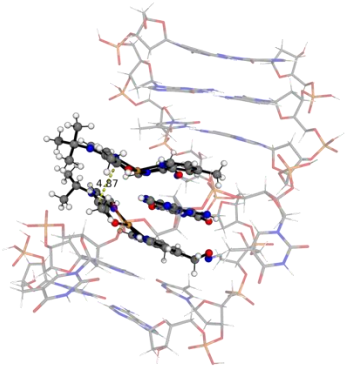
***o*-CC'**	***n*-CC'**
ΔΔE = 19.7 kcal/mol	N/C
d = 6.28 Å	*d* = 8.34 Å
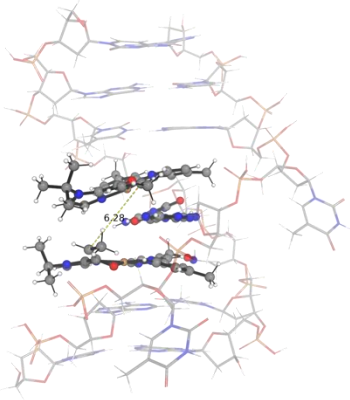	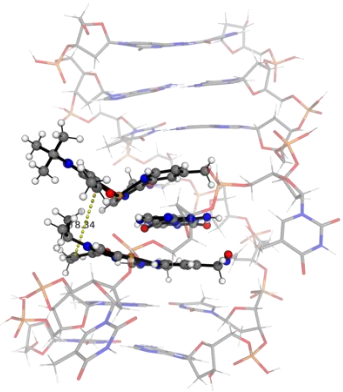
***o*-C'A**	***n*-C'A**
N/C	ΔΔE = 13.4 kcal/mol
d = 10.79 Å	*d* = 4.63 Å
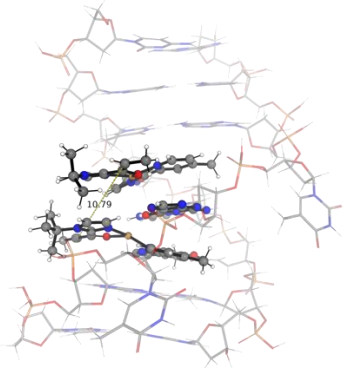	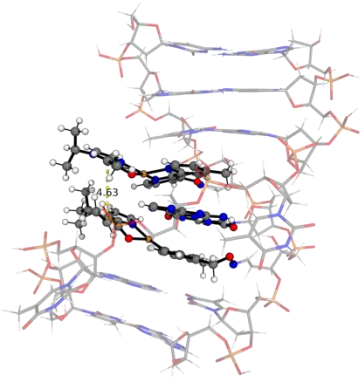
***o*-C'C**	***n*-C'C**
ΔΔE = 27.6 kcal/mol	N/C
d = 6.71 Å	*d* = 8.28 Å

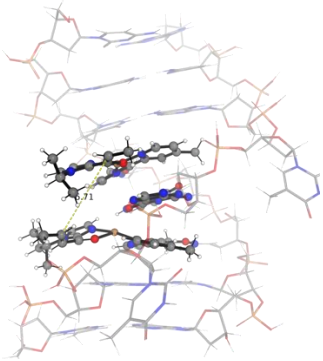	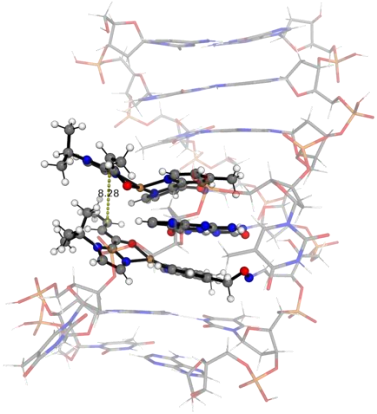
***o*-DB'**	***o*-DD'**
ΔΔE = 10.9 kcal/mol	N/C
d = 5.80 Å	*d* = 9.36 Å
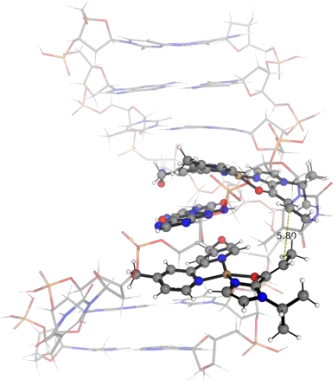	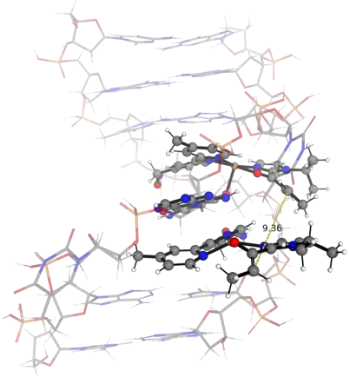
***o*-D'B**	***o*-D'D**
ΔΔE = 56.0 kcal/mol	N/C
d = 5.57 Å	*d* = 11.13 Å
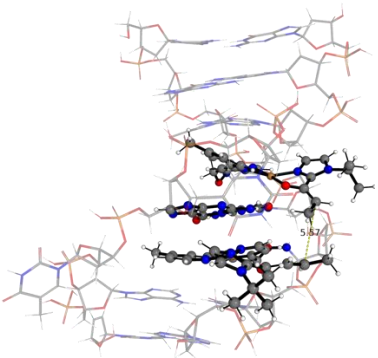	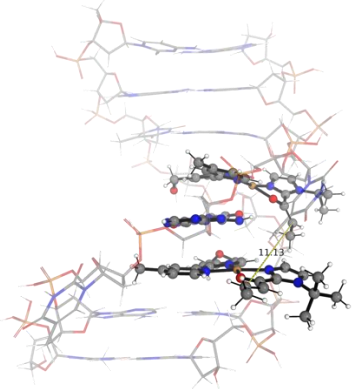

Figure S7. GFN2-xTB-optimized reactant states of the reaction. Relative energy values are given in kcal/mol with respect to the most stable complex. N/C denotes "not calculated" due to the unfeasible geometrical arrangement for product formation.

4 xTB-optimized structures

Geometries of all xTB-optimized structures (in *.xyz* format) are included in a folder named *final_structures* with an associated *readme.txt* file. All these data have been uploaded to zenodo.org (https://zenodo.org/records/16626042) with DOI: 10.5281/zenodo.16626042.

References:

1. Sheng, J. *et al.* Merging DNA repair with bioorthogonal conjugation enables accessible and versatile asymmetric DNA catalysis. *J. Am. Chem. Soc.* **146**, 16531–16539 (2024).
2. Duchemin, N. *et al.* New benchmark in DNA-based asymmetric catalysis: Prevalence of modified DNA/RNA hybrid systems. *J. Am. Chem. Soc. Au* **2**, 1910–1917 (2022).
3. Evans, D. A. & Fandrick, K. R. Catalytic enantioselective pyrrole alkylations of α,β-unsaturated 2-acyl imidazoles. *Org. Lett.* **8**, 2249–2252 (2006).
4. Gong, J., Wan, Q. & Kang, Q. Enantioselective Mukaiyama–Michael reaction catalyzed by a chiral rhodium complex based on pinene-modified pyridine ligands. *Chem. Asian J.* **13**, 2484–2488 (2018).
5. Tanaka, T., Tanaka, T., Tsuji, T., Yazaki, R. & Ohshima, T. Strategy for catalytic chemoselective cross enolate coupling reaction via a transient homocoupling dimer. *Org. Lett.* **20**, 3541–3544 (2018).
6. Tan, Y., Yuan, W., Gong, L. & Meggers, E. Aerobic asymmetric dehydrogenative cross-coupling between two C(sp^3)–H groups catalyzed by a chiral-at-metal rhodium complex. *Angew. Chem. Int. Ed.* **54**, 13045–13048 (2015).
7. Deng, T., Bora, P. P., Lin, S.-X., Li, Y. & Kang, Q. Octahedral iridium complex catalyzed α-chlorination of 2-acyl imidazoles with tosyl chloride. *Tetrahedron Lett.* **58**, 1102–1106 (2017).
8. Bora, P. P., Sun, G.-J., Zheng, W.-F. & Kang, Q. Rh/Lewis acid catalyzed regio-, diastereo- and enantioselective addition of 2-acyl imidazoles with allenes. *Chin. J. Chem.* **36**, 20–24 (2018).
9. Zhang, Q., Chang, X., Peng, L. & Guo, C. Asymmetric Lewis acid catalyzed electrochemical alkylation. *Angew. Chem. Int. Ed.* **58**, 6999–7003 (2019).
10. Ren, Y., Lu, S., He, L., Zhao, Z. & Li, S.-W. Catalytic asymmetric decarboxylative Michael addition to construct an all-carbon quaternary center with 3-alkenyl-oxindoles. *Org. Lett.* **24**, 2585–2589 (2022).
11. Huang, Y., Song, L., Gong, L. & Meggers, E. Asymmetric synthesis of hydrocarbazoles catalyzed by an octahedral chiral-at-rhodium Lewis acid. *Chem. Asian J.* **10**, 2738–2743 (2015).
12. Evans, D. A., Fandrick, K. R., Song, H.-J., Scheidt, K. A. & Xu, R. Enantioselective Friedel–Crafts alkylations catalyzed by bis(oxazolinyl)pyridine–Sc(III) complexes. *J. Am. Chem. Soc.* **129**, 10029–10041 (2007).
13. Qurban, S., Du, Y., Gong, J., Lin, S. & Kang, Q. Enantioselective synthesis of tetrahydroisoquinoline derivatives via chiral-at-metal rhodium complex catalyzed [3+2] cycloaddition. *Chem. Commun.* **55**, 249–252 (2019).
14. Pang, B., Xin, H.-L., Choi, J., Morimoto, H. & Ohshima, T**.** $Sc(OTf)_3$-catalyzed C–C bond cleavage of unactivated acylazaarenes with 1,2-diamines to afford azaarenes and imidazoles. *Org. Lett.* **27**, 2075–2080 (2025).

15. Li, K. & Meggers, E. Chiral-at-metal Rh(III) complex catalyzed asymmetric conjugate addition. *Org. Lett.* **19**, 3299–3302 (2017).
16. Liubo Li, Xinyi Wang & Niankai Fu. Electrochemical Ni-catalyzed hydrogenation of alkenes. *Angew. Chem.* **136**, (22), e202403475 (2024).
17. Xin, H.-L., Pang, B., Choi, J., Akkad, W., Morimoto, H. & Ohshima, T. C–C bond cleavage of unactivated 2-acylimidazoles. *J. Org. Chem.* **85**, 11592–11606 (2020).
18. Lu, P., Jackson, J. J., Eickhoff, J. A. & Zakarian, A. Direct enantioselective conjugate addition of carboxylic acids with chiral lithium amides as traceless auxiliaries. *J. Am. Chem. Soc.* **137**, 656–659 (2015).
19. Bannwarth, C., Ehlert, S. & Grimme, S. GFN2-xTB — an accurate and broadly parametrized self-consistent tight-binding quantum chemical method with multipole electrostatics and density-dependent dispersion contributions. *J. Chem. Theory Comput.* **15**, 1652–1671 (2019).
20. Grimme, S., Bannwarth, C. & Shushkov, P. A robust and accurate tight-binding quantum chemical method for structures, vibrational frequencies, and noncovalent interactions of large molecular systems parametrized for all spd-block elements (Z = 1–86). *J. Chem. Theory Comput.* **13**, 1989–2009 (2017).
21. Bannwarth, C. *et al.* Extended tight-binding quantum chemistry methods. *WIREs Comput. Mol. Sci.* **11**, e1493 (2021).
22. Frisch, M. J. *et al.* Gaussian 16, Revision C.01. Gaussian Inc., Wallingford, CT (2016).
23. Becke, A. D. Density-functional thermochemistry. III. The role of exact exchange. *J. Chem. Phys.* **98**, 5648–5652 (1993).
24. Perdew, J. P. Density-functional approximation for the correlation energy of the inhomogeneous electron gas. *Phys. Rev. B* **33**, 8822–8824 (1986).
25. Grimme, S., Antony, J., Ehrlich, S. & Krieg, H. A consistent and accurate ab initio parametrization of density functional dispersion correction (DFT-D) for the 94 elements H–Pu. *J. Chem. Phys.* **132**, 154104 (2010).
26. Becke, A. D. & Johnson, E. R. Exchange-hole dipole moment and the dispersion interaction. *J. Chem. Phys.* **122**, 154104 (2005).
27. Johnson, E. R. & Becke, A. D. A post-Hartree–Fock model of intermolecular interactions. *J. Chem. Phys.* **123**, 024101 (2005).
28. Johnson, E. R. & Becke, A. D. A post-Hartree–Fock model of intermolecular interactions: inclusion of higher-order corrections. *J. Chem. Phys.* **124**, 174104 (2006).
29. Becke, A. D. & Johnson, E. R. A density-functional model of the dispersion interaction. *J. Chem. Phys.* **123**, 154101 (2005).
30. Ditchfield, R., Hehre, W. J. & Pople, J. A. Self-consistent molecular-orbital methods. IX. An extended Gaussian-type basis for molecular-orbital studies of organic molecules. *J. Chem. Phys.* **54**, 724–728 (1971).

31. Yu, H. S., He, X., Li, S. L. & Truhlar, D. G. MN15: a Kohn–Sham global-hybrid exchange–correlation density functional with broad accuracy for multi-reference and single-reference systems and noncovalent interactions. *Chem. Sci.* **7**, 5032–5051 (2016).
32. Guin, S. *et al.* Iterative arylation of amino acids and aliphatic amines via δ-C(sp³)–H activation: experimental and computational exploration. *Angew. Chem. Int. Ed.* **58**, 5633–5638 (2019).
33. Achar, T. K. *et al.* Palladium-catalyzed directed meta-selective C–H allylation of arenes: unactivated internal olefins as allyl surrogates. *Angew. Chem. Int. Ed.* **58**, 10353–10360 (2019).
34. Porey, S. *et al.* Alkyne linchpin strategy for drug:pharmacophore conjugation: experimental and computational realization of a meta-selective inverse Sonogashira coupling. *J. Am. Chem. Soc.* **142**, 3762–3774 (2020).
35. Sinha, S. K. *et al.* Dual ligand enabled nondirected C–H chalcogenation of arenes and heteroarenes. *J. Am. Chem. Soc.* **144**, 12032–12042 (2022).
36. Das, J. *et al.* Access to unsaturated bicyclic lactones by overriding conventional C(sp³)–H site selectivity. *Nat. Chem.* **15**, 1626–1635 (2023).
37. Porey, S., Bairagi, Y., Guin, S., Zhang, X. & Maiti, D. Nondirected C–H/C–F coupling for the synthesis of α-fluoro olefinated arenes. *ACS Catal.* **13**, 14000–14011 (2023).
38. Bairagi, Y., Porey, S., Vummaleti, S. V. C., Zhang, X., Lahiri, G. K. & Maiti, D. Synthesis of β-(hetero)aryl ketones via ligand-enabled nondirected C–H alkylation. *ACS Catal.* **14**, 15654–15664 (2024).
39. Dutta, U., Prakash, G., Devi, K., Borah, K., Zhang, X. & Maiti, D. Directing group assisted para-selective C–H alkynylation of unbiased arenes enabled by rhodium catalysis. *Chem. Sci.* **14**, 11381–11388 (2023).
40. Marenich, A. V., Cramer, C. J. & Truhlar, D. G. Universal solvation model based on solute electron density and on a continuum model of the solvent defined by the bulk dielectric constant and atomic surface tensions. *J. Phys. Chem. B* **113**, 6378–6396 (2009).
41. Reginsson, G. W. & Schiemann, O. Studying biomolecular complexes with pulsed electron–electron double resonance spectroscopy. *Biochem. Soc. Trans.* **39**, 128–139 (2011).
42. Chiang, C.-Y. *et al.* Copper-dependent halogenase catalyses unactivated C–H bond functionalization. *Nature* **638**, 126–132 (2025).
43. Schrödinger, LLC. *The PyMOL Molecular Graphics System*, version 1.8 (2015).